Article

Multiparametric Apparatus for Real-Time Observations of Volcanic Aerosol Optical and Microphysical Properties at Etna (Italy): Calibration Procedures and Measurement Tests

Matteo Manzo , Gianpiero Aiesi , Antonella Boselli * , Salvatore Consoli , Riccardo Damiano ,
Guido Di Donfrancesco , Benedetto Saraceno , Simona Scollo

Posted Date: 29 January 2024

doi: 10.20944/preprints202401.1976.v1

Keywords: Lidar; Aerosol parameters; Calibration.

Preprints.org (www.preprints.org) | NOT PEER-REVIEWED | Posted: 29 January 2024 doi:10.20944/preprints202401.1976.v1

Article

Multiparametric Apparatus for Real-Time Observations of Volcanic Aerosol Optical and Microphysical Properties at Etna (Italy): Calibration Procedures and Measurement Tests

Matteo Manzo [1], Gianpiero Aiesi [2], Antonella Boselli [3,*], Salvatore Consoli [2], Riccardo Damiano [1], Guido Di Donfrancesco [4], Benedetto Saraceno [2] and Simona Scollo [2]

[1] Dipartimento di Fisica "Ettore Pancini" Università di Napoli Federico II, Complesso Universitario di Monte S. Angelo, I-80126 Napoli, Italy; matteo.manzo@unina.it
[2] Istituto Nazionale di Geofisica e Vulcanologia, Osservatorio Etneo, Piazza Roma 2, 95125 Catania, Italy; salvatore.consoli@ingv.it; gianpiero.aiesi@ingv.it; benedetto.saraceno@ingv.it; simona.scollo@ingv.it
[3] IMAA-CNR Istituto di Metodologie per l'Analisi Ambientale, Consiglio Nazionale delle Ricerche, I-85050 Tito Scalo-Potenza, Italy; antonella.boselli@cnr.it
[4] Agenzia Nazionale per le nuove tecnologie, l'energia e lo sviluppo economico sostenibile ENEA – Unità tecnica Antartide C.R. Casaccia – Roma, Italy; guido.didonfrancesco@enea.it
* Correspondence: antonella.boselli@cnr.it

Abstract: An innovative mobile Lidar device, developed to monitor volcanic plumes during explosive eruptions at Mt. Etna (Italy) and analyze the optical properties of volcanic particles was upgraded in October 2023 with the aim to improve volcanic plume retrievals. The new configuration of the lidar allows to obtain new data of both the optical and the microphysical properties of the atmospheric aerosol. In fact, after its upgrade, the lidar has the possibility to measure 3β, 2α and 2δ in a configuration defined as "state of the art lidar" where properties such as the particle size distribution and refractive index can be derived. During the lidar implementation we were able to to test the system performance through specific calibration measurements. In this work, the first measurement results are shown and compared with results obtained by other instruments aimed at proving the ability of the upgraded system to more precisely characterize the aerosol optical and microphysical properties.

Keywords: lidar; aerosol parameters; calibration

1. Introduction

During explosive eruptions, volcanic plumes, containing particles of different size and composition named tephra, rise at high speed and are dispersed into the atmosphere. Those particles can constitute one of the most important volcanic hazards. In fact, tephra is dangerous for aviation operations causing, in the worst case, aircraft engine failure [1]. Moreover, tephra fallout can affect some infrastructures [2] and cause health diseases [3]. Fine volcanic ash (tephra having a size less than 63 μm), blowing with the winds, can reach long distances (in the order of several kilometres) affecting also areas far away from the eruptive vents [4] and involving different countries. Mainly for those reasons, the quantification of volcanic ash concentration and tephra load in atmosphere is very important. These are usually provided by volcanic ash advisory centres (VAACs) or by volcano observatories [5] using volcanic ash transport and deposition models (VATDM). However, the VATDMs require the estimation of eruption source parameters and, consequently, volcanological observations are needed.

Measurements of eruption source parameters using different systems surrounding active volcanoes are crucial. The main eruption source parameters are column height, mass eruption rate (or total mass) and total grain-size distribution. The column height is the easiest to detect by means of remote sensing systems, spanning from visual observations and satellite images to radar [6] and lidars [7]. Instead, although mass eruption rate has a first order effect on dispersal and sedimentation, it is difficult to detect in real time and larger uncertainties still now remain using inversion models [8]. Furthermore, measurements of the whole size spectrum of particles ejected during an eruption are possible only using remote sensing systems at different wavelengths. As those measurements are very difficult, the whole grain-size distribution is often assumed to be equal to some past eruptions or based on an average of measurements made in volcanic plumes [9].

During last years, Lidar measurements have become a valuable tool for monitoring volcanic plumes. As an example, Lidar measurements from different sites were available during the 2010 Eyjafjallajökull eruption [9–12] and during the 2002 Etna eruptions [13]. Lidar network allowed to estimate important features of volcanic plume dispersal such as the 4D distribution in the troposphere over Europe and its optical properties [14]. At Etna, lidar measurements have been carried out since 2010, initially using a single-wavelength lidar prototype [15] and then using a more complex multi-wavelength system [16]. Those measurements allowed for the first time to measure the Lidar ratio during an event and have more reliable estimates of volcanic ash concentration. The system has been recently updated to provide more detailed information on volcanic plumes at Etna. In this paper we describe the improvements of such a system, its new calibration measures and future capabilities.

2. Materials and Methods

The VULCAMED project, developed under the National Operational Programme "Research and Competitiveness" 2007–2013, aimed at increasing the structural strengthening of research centers such as the Istituto Nazionale di Geofisica e Vulcanologia (INGV) for improving studies of high-risk volcanic areas and their geothermal potential in the Mediterranean. In the frame of the VULCAMED project, an innovative lidar system was developed. The lidar at first was designed to make measurements in the UV (355 nm, 386 nm) and IR (1530 nm) spectral regions but successively, in 2023, it has been upgraded adding elastic channels at 1064 nm and 532 nm, the N_2 Raman channel at 607 nm and the H_2O Raman channel at 407 nm thanks to the INGV funds of PON-GRINT. Moreover, the parallel and perpendicularly polarized components (P and S) of the elastic signals at 355 and 532 nm have been added in order to have a more accurate estimation of the detected aerosol, retrieving information about their shape. These new system features allow a complete aerosol characterization during volcanic activity.

The lidar system is based on a compact diode pumped and air-cooled Nd:YAG laser (WEDGE model specifically developed by Bright Solutions s.r.l.). The laser simultaneously emits 3 different wavelengths: the fundamental (1064 nm), the second (532 nm) and third harmonics (355 nm), with 1 KHz repetition rate; the corresponding averaged optical powers are 1W, 1.5W and 0.6 W, respectively.

A Cassegrain telescope in Dall-Kirkham configuration with a 25 cm diameter and F number 4.5 collects the backscattered radiation which is then spectrally separated by means of beam splitters and dichroic mirrors in an eight-channel polychromator unit. Moreover, the system allows to perform polarization measurements at both 355 and 532 nm. In order to accomplish this measure, polarizing beam splitters are located inside the polychromator unit to split the light into parallel and perpendicularly polarized components (P and S). Narrow bandpass filters produced by ALLUXA are located in front of the detectors and allow to select specific wavelengths. The signals are then detected, for each channel, using photomultipliers tubes (Hamamatsu H10721P-210 for 355, 386, 407, 532 nm and H16721 for 607 nm), except for the 1064 nm channel where an avalanche photodiode (APD-3.0 LICEL) in analog regime is used. The experimental set-up of the polychromator unit of the lidar is illustrated in Figure 1.

Preprints.org (www.preprints.org) | NOT PEER-REVIEWED | Posted: 29 January 2024 doi:10.20944/preprints202401.1976.v1

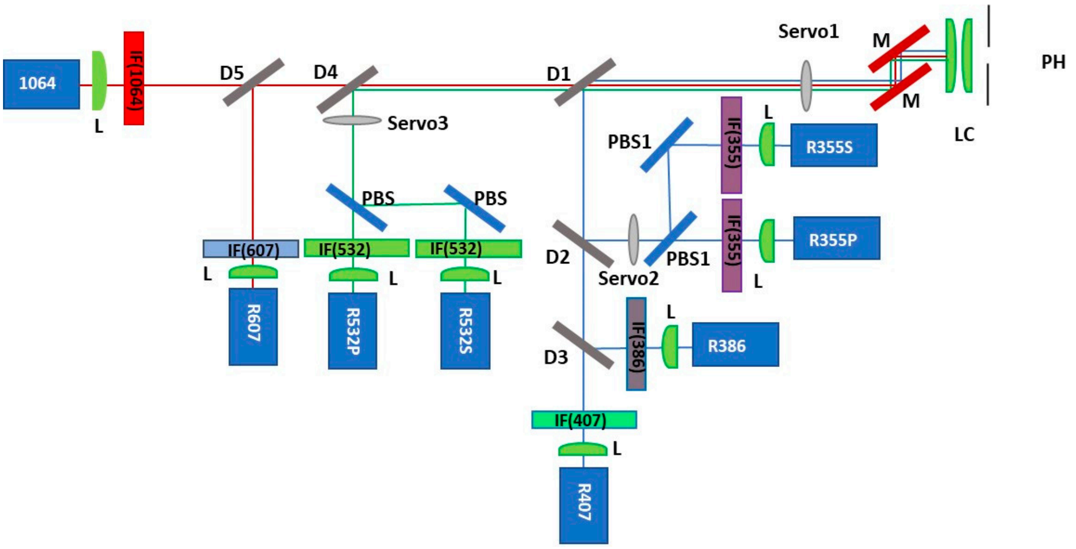

Figure 1. Experimental set-up of the polychromator unit after the lidar system upgrade: P stays for 'Pinhole', M for 'Mirror', D for 'Dichroic mirror', PBS for 'Polarizing Beam Splitter', L for 'Lens', IF (λ nm) for 'Interferential Filter'. The servo (1-3) are used to insert the attenuators or the depolarizer plates along the optical path. .

Each detected signal is then processed by a sophisticated data acquisition system (ALA CLASS Configurable Lidar Acquisition SyStem) designed by ALA Advanced Lidar Applications s.r.l. to give great performances, including a motherboard and independent acquisition modules for photo-counting. A single electronic board (ALA LARA LidAR controlleR board), provided with an intuitive and user-friendly software, allows to manage the Lidar system.

Optical properties of aerosol such as the backscattering coefficient (β), the extinction coefficient (α) and the aerosol depolarization ratio (δ) are retrieved from the lidar data using inversion algorithms. In particular, β was obtained using two different methods: the Klett-Fernald [17,18] for diurnal measurements, when only elastic signals are available, and the Elastic/Raman method [19] for measurements carried out after the sunset. Using the first method, an assumption on the ratio between α and β, the Lidar Ratio LR, is needed. The α was retrieved using the inversion method proposed by Ansmann [20], while δ is calculated using the ratio between P and S backscattering coefficients [21]. Finally, information about the water vapor mixing ratio was obtained from the 407 nm Raman signal using the correspondent N_2 Raman signal as a reference [22,23].

The new configuration of the lidar, with the capability to measure 3β, 2α and 2δ, allows to retrieve optical and microphysical properties of the aerosol. So, the upgrade brought the lidar to a configuration definable as "state of the art lidar" according to [24], when properties such as volume particle size distribution and refractive index of the particles can be derived.

3. Results

3.1. Calibration methods

The optimization of the results achieved from a lidar instrument depends on the implementation of specific tests to establish the system performances and define a number of technical parameters allowing to reduce the uncertainty on the retrieved profiles. In order to make accurate measurements of the aerosol optical and microphysical properties, the lidar system should then be calibrated. The system calibration concerned different issues: the check of the lidar signal dynamic range; the measurement of the Gain ratio (G) for the depolarization calibration and of the overlap function (O(z)) to correct the lidar signal at lower altitudes; the analysis of the near range signal to test the optical and optomechanical design of the lidar receiver; the multiwavelength channels calibration.

doi:10.20944/preprints202401.1976.v1

3.1.1. Rayleigh fit test

The comparison between the lidar profile and the one expected from a pure molecular atmosphere, the latter derived from the air density and temperature profiles by nearby radiosounding or by standard atmosphere look-up table, allows to verify the correct dynamics of the lidar signal. The procedure, known as Rayleigh fit test, is based on the normalization between the two profiles in clear atmospheric conditions and it is used in the lidar data pre-processing in order to check the correct background noise to be subtracted from the signal before the data retrieval.

A comparison between the Range Corrected Signal (RCS-black line) of the lidar and the molecular profile (blue line) at the three different wavelengths (355, 532 and 1064 nm) is reported in Figures 2a, 3a and 4a; Figures 2b,3b,4b report the relative difference between them. Lidar signals were normalized to the molecular profiles in the region between 7.2 km and 12 km and for all the 3 wavelengths the relative differences between them are around zero, highlighting the correct lidar signal dynamics.

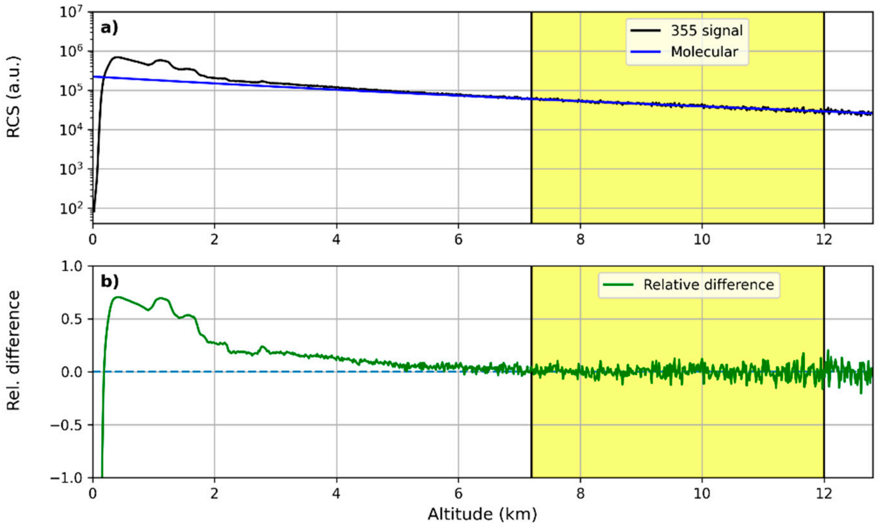

Figure 2. Results of Rayleigh fit tests for the 355nm wavelength: a) fit between the Range Corrected lidar Signal (RCS) and a pure molecular profile; b) relative differences between the RCS and the pure molecular profile.

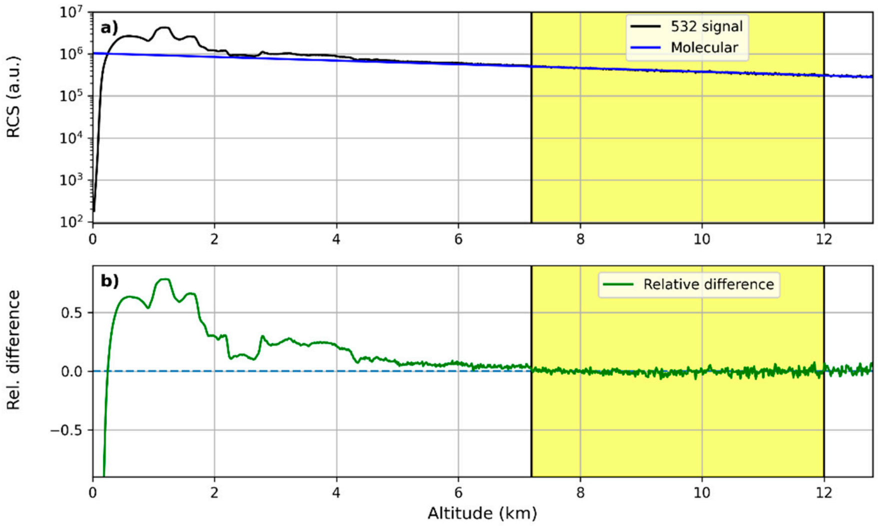

Figure 3. Results of Rayleigh fit tests for the 532nm wavelength: a) fit between the Range Corrected lidar Signal (RCS) and a pure molecular profile; b) relative differences between the RCS and the pure molecular profile.

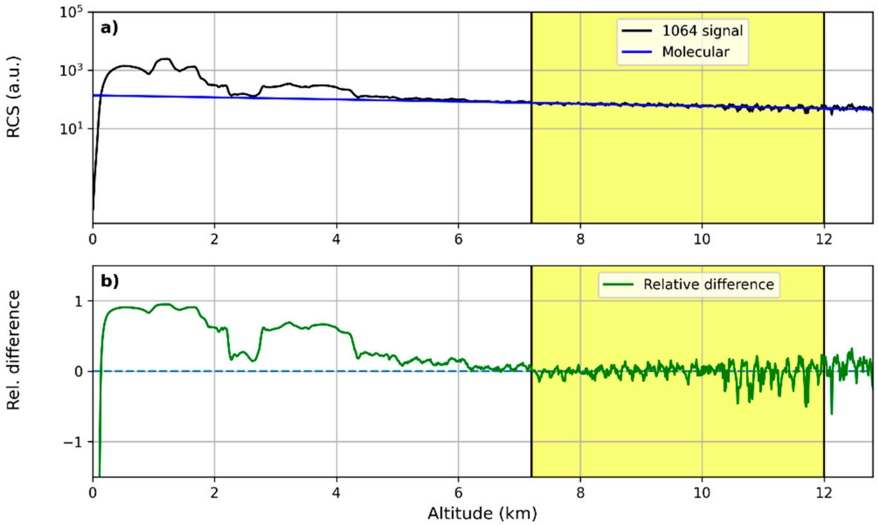

Figure 4. Results of Rayleigh fit tests for the 1064nm wavelength: a) fit between the Range Corrected lidar Signal (RCS) and a pure molecular profile; b) relative differences between the RCS and the pure molecular profile.

3.1.2. Depolarization calibration

The lidar is capable to detect the two parallel (P) and perpendicular (S) components of the signal with respect to the polarization plane of the emitted laser beam, on both the 355 nm and 532 nm wavelengths. A depolarization calibration procedure is needed to estimate the gain factor between these two lidar channels for each wavelength.

The parameter G, called gain ratio, depends on the gain difference between the two channels and it must be measured to retrieve the corrected aerosol depolarization ratio δ [21,25,26].

The depolarization calibration was obtained placing a depolarizer plate inside the polychromator unit along the optical path of each of the two branches corresponding to 355 nm and 532 nm, in order to make the backscattered light fully unpolarized. In addition, due to the not perfectly polarized light coming out from the laser and the various optical components on the beam optical path that can introduce a depolarization factor, a correction using pure molecular scattering profile is needed.

This calibration method followed the two steps procedure detailed in [27]: firstly, the gain ratio between the two channels was evaluated, then the correction of instruments depolarization is achieved using pure molecular scattering profiles, normalizing the gain ratio to an appropriate value known from the theory [25].

As shown in Figure 5, the mean value of δ at 355 nm and at altitude between 8 km and 14 km, corresponding to an aerosol free region, was equal to (0.51±0.11)% in agreement with the expected depolarization of 0.5% for a pure molecular scattering signal according to the bandwidth of the used interference filter [25].

doi:10.20944/preprints202401.1976.v1

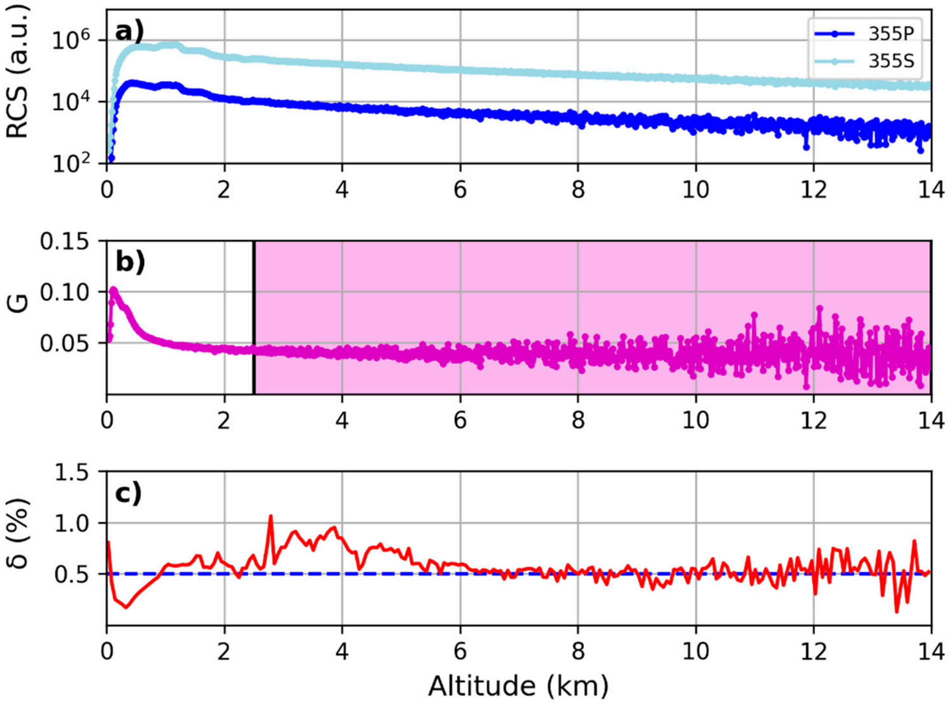

Figure 5. Results for the depolarization calibration @ 355 nm: (**a**) comparison between P and S signals in a series of measurements with the depolarizer plate; (**b**) gain ratio @ 355 nm; (**c**) total depolarization ratio percentage @ 355 nm. The average value of δ is about 0.5% in the aerosol-free region 8-14 km.

The same procedure has been done for the 532 channels (Figure 6). In this case, the mean δ value in the free-aerosol range 8-14 km resulted (0.32±0.05) % that is comparable, within the errors, to the value of 0.365 % expected from the theory for pure molecular scattering signal at 532 nm, according to the bandwidth of the used interference filters [25].

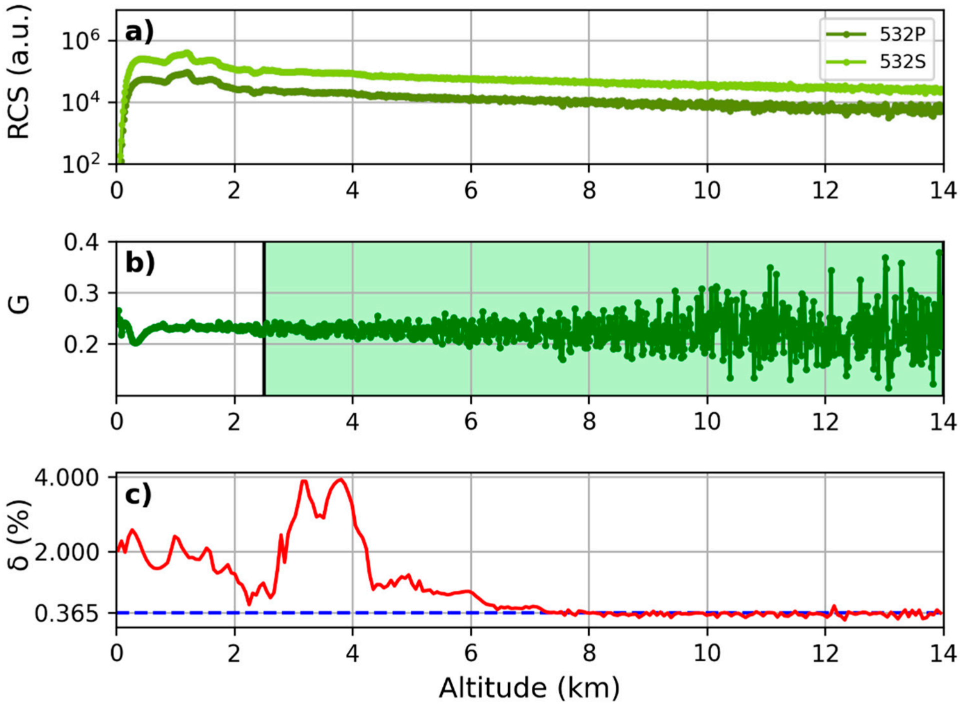

doi:10.20944/preprints202401.1976.v1

Figure 6. Results for the depolarization calibration @ 532 nm: (**a**) comparison between P and S signals in a series of measurements using the depolarizer plate; (**b**) gain ratio @ 532 nm; (**c**) total depolarization ratio percentage @ 532 nm. The average value of δ is about 0.37% in the aerosol-free region 8 -14 km.

3.1.3. Overlap function

The lidar signal coming from altitudes close to the ground is underestimated because, for a bistatic lidar, the incomplete overlap between the laser beam and the telescope's field of view (FOV). Correcting the signal with the overlap function down to very low altitudes allows to obtain useful data that can be used for lower atmosphere investigations and air quality control.

To determine the overlap function, among other possible methods [27–30], an iterative method has been applied using both Raman and Elastic backscattered signals. Here we make the assumption that the lidar ratio is constant within the first kilometers of the atmosphere or, in other words, that the aerosol typology does not change. The used method is detailed in [27]. Figures 7a and 8a show the overlap function which affects the aerosol backscattering profiles derived by the Klett inversion method (red line in the figures); in a different way, the aerosol backscattering coefficient retrieved from the ratio between the elastic and Raman lidar profiles (blue line in the figure) is not dependent on the overlap function. The iterative procedure allowed to correct the aerosol profile for the overlap function after just two iterations and, as expected, both the derived backscattering profiles resulted superimposed (Figures 7b and 8b).

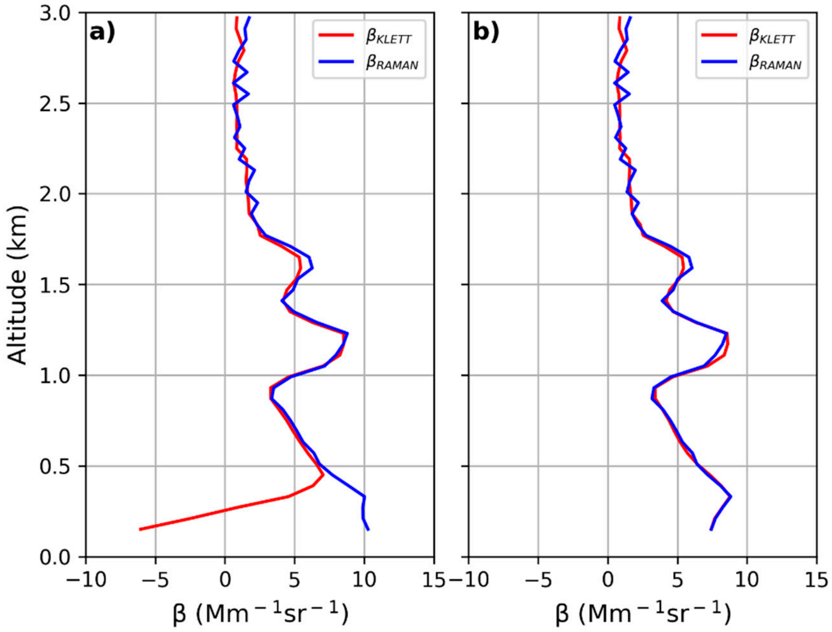

Figure 7. Comparison between β_{KLETT} and β_{RAMAN} @ 355 nm before and after overlap correction: (**a**) backscattering coefficients before overlap correction; (**b**) backscattering coefficients matching just after 2 iterations of the method.

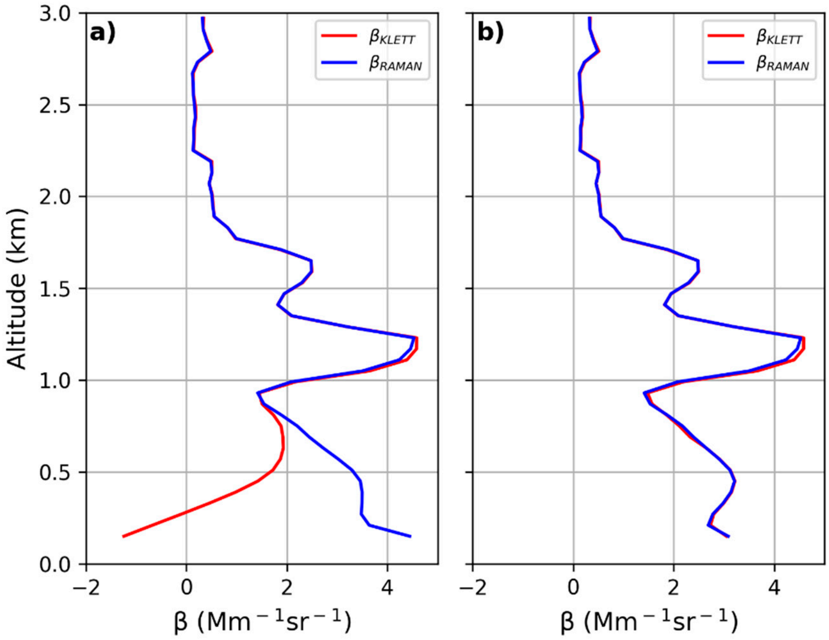

Figure 8. Comparison between βKLETT and βRAMAN @ 532 nm before and after overlap correction: (**a**) backscattering coefficients before overlap correction; (**b**) backscattering coefficients matching after 2 iterations of the method.

The lidar signals, before and after the overlap correction was applied, are reported in Figures 9a and 10a at 532 nm and 355 nm, respectively. The corresponding overlap functions, as resulting from the iterative procedure, are displayed in panel b) of each figure: a full overlap height of 580 m for the lidar signal at 355 nm and of 900 m for the lidar signal at 532 nm are obtained.

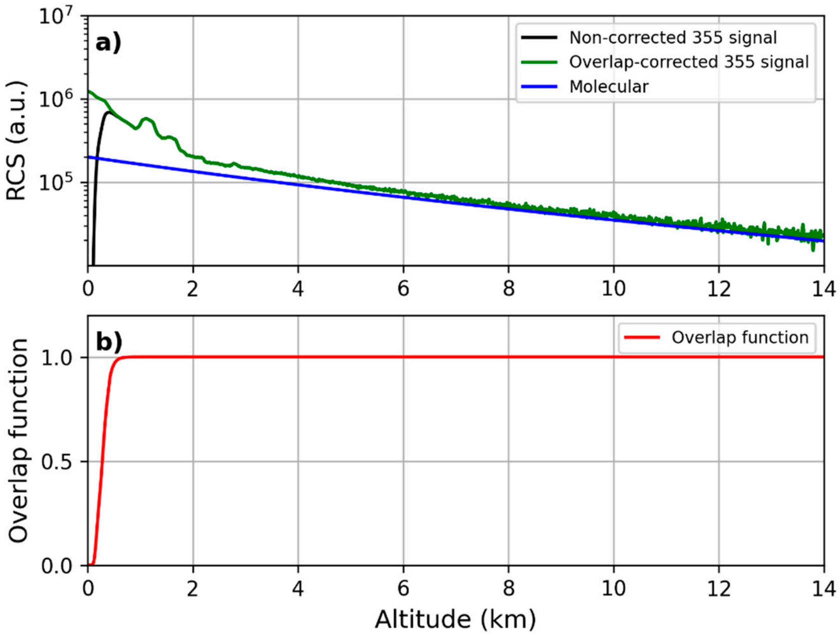

Figure 9. Comparison between RCS @ 355 nm before and after the overlap correction: (**a**) non-corrected RCS @ 355 nm; (**b**) overlap-corrected RCS @ 355 nm; (**c**) overlap function @ 355 nm.

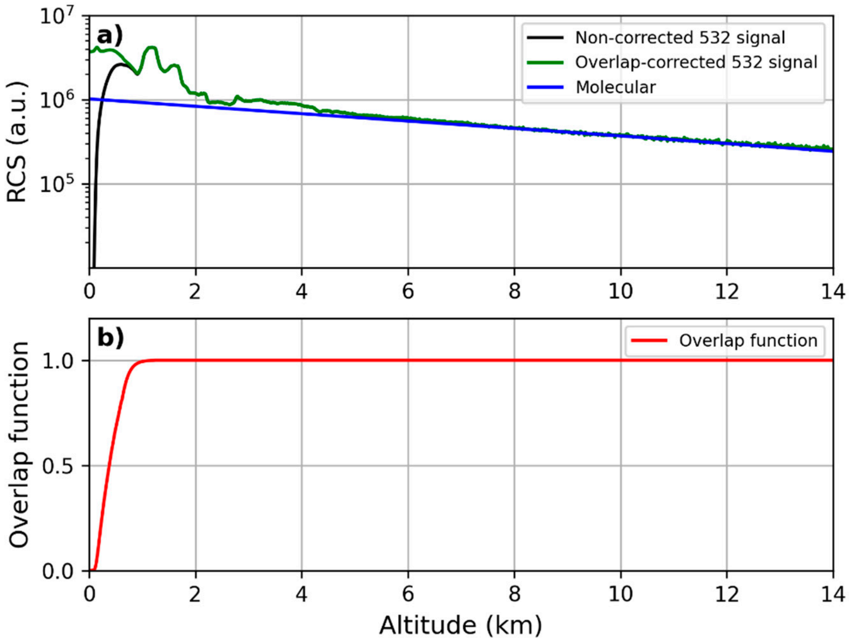

Figure 10. Comparison between RCS @ 532 nm before and after the overlap correction: (**a**) non-corrected RCS @ 532 nm; (**b**) overlap-corrected RCS @ 532 nm; (**c**) overlap function @ 532 nm.

3.1.4. Telecover test

The specific Telecover test allows to verify the correct alignment between the laser beam and the receiver optical chain by checking the signal received from the different quadrants of the telescope.

The Rayleigh fit works in the far-range where it is likely to find a portion of the lidar profile in clear air. Unlike there is no calibration method for near-range, where the lidar profile is likely characterized by a stable presence of urban and natural pollution. Unfortunately it is at low altitudes that the effects of misalignments and shortcomings of the optics show at the most [31]. To overcome this problem, it is necessary to perform a test in which lidar signals acquired using different sectors of the telescope are compared. If the optical alignment of the lidar system is correct, it is expected that signals from different sectors don't show any difference after normalization. The comparison hence suggests a quote below which the overlap function becomes relevant.

The method used in this work is the Quadrant-test [31], where the telescope is covered in such a way that only a quarter at a time of it is used. Every measurement has a duration of 15 min for each quarter of telescope, repeating the measure of first quadrant at the end for taking into account any change in the atmospheric profile during the test.

The results of the Telecover-test for the lidar are reported in Figure 11.

Normalized Lidar signals didn't show difference at higher altitudes suggesting that the distance of full overlap at 355 and 532 nm is the one estimated in section 3.1.3. The same figure suggested that the 1064 nm signal have a full overlap at about 900 m, similarly to the 532 nm channel.

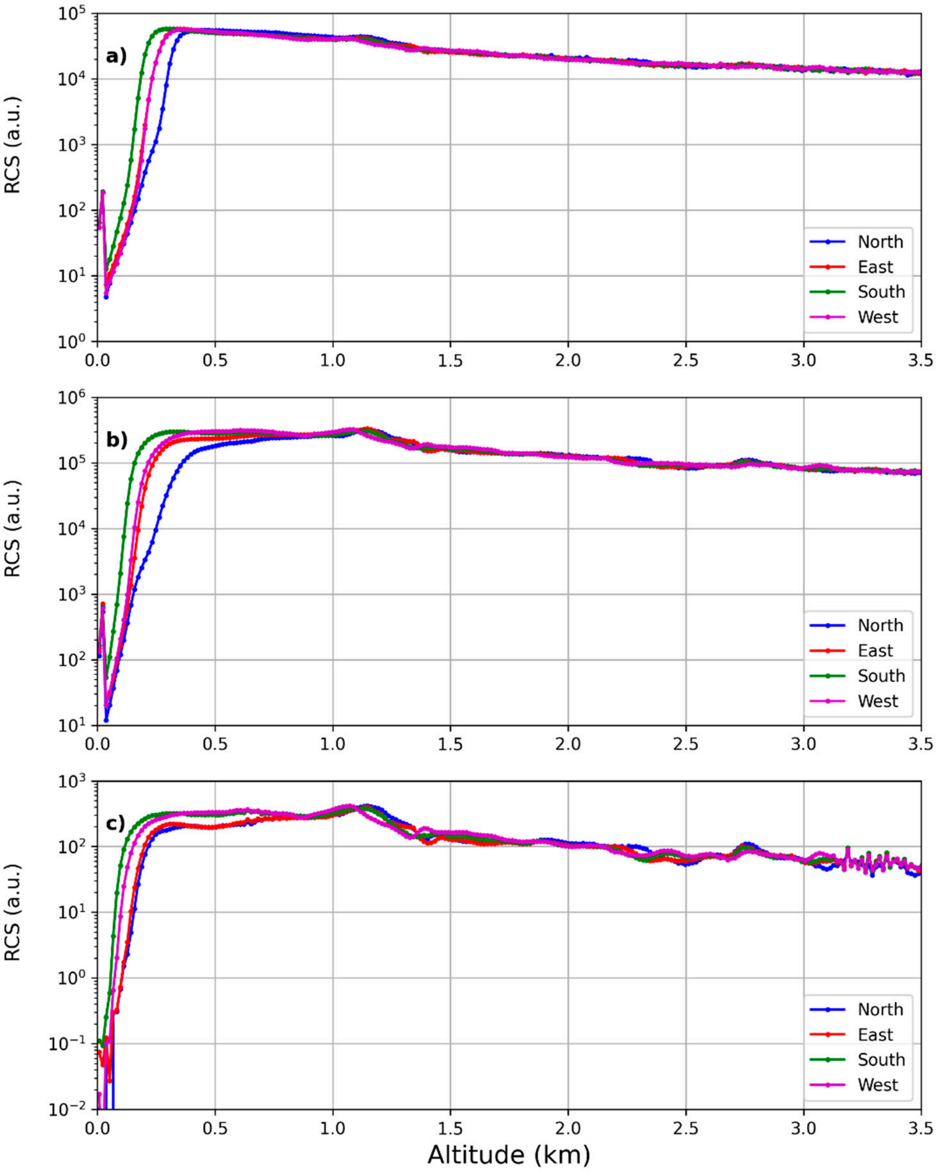

Figure 11. The telecover test at 355 nm (a) 532 nm (b) and 1064 nm (c). The different colours identify different sectors of the telescope.

3.1.5. Channel calibration

In order to verify the correct wavelength dependence of the measured optical parameters, we calculated the backscatter-related Angstrom exponents (BAE) measured at the different wavelengths.

This parameter is expressed as:

$$BAE = -\frac{\log\left(\frac{\beta(\lambda_i)}{\beta(\lambda_j)}\right)}{\log\left(\frac{\lambda_i}{\lambda_j}\right)}$$

where $\lambda_{i/j}$ are the emitted wavelengths (355, 532 and 1064 nm) and β are the corresponding aerosol backscattering parameters.

A lidar profile characterized by a thin cirrus cloud is a good test to verify that, inside of a layer, the calculated BAEs at each of the three wavelengths show the same value, being the backscattering coefficient independent on the wavelength [32]. For this purpose, Lidar measurements carried out on October 5, 2023 from 17:30 to 18:00 UTC, showing a cirrus at about 15 km of altitude, were used. The vertical and temporal resolution of the measure was of 15 m and 60 s, respectively. Figure 12 reports the colour maps of the range corrected lidar signals showing the spatio-temporal variation of the aerosol layering observed in the atmosphere at the three wavelengths. The corresponding backscattering coefficients at each wavelength, retrieved with a spatial resolution of 30 m, are reported in Figure 13. The profiles at different wavelengths appear superimposed in the atmospheric range between 14 and 16 km, as expected the 3 BAE values summarized in Table 1, resulted comparable with zero, hence showing a correct calibration between channels.

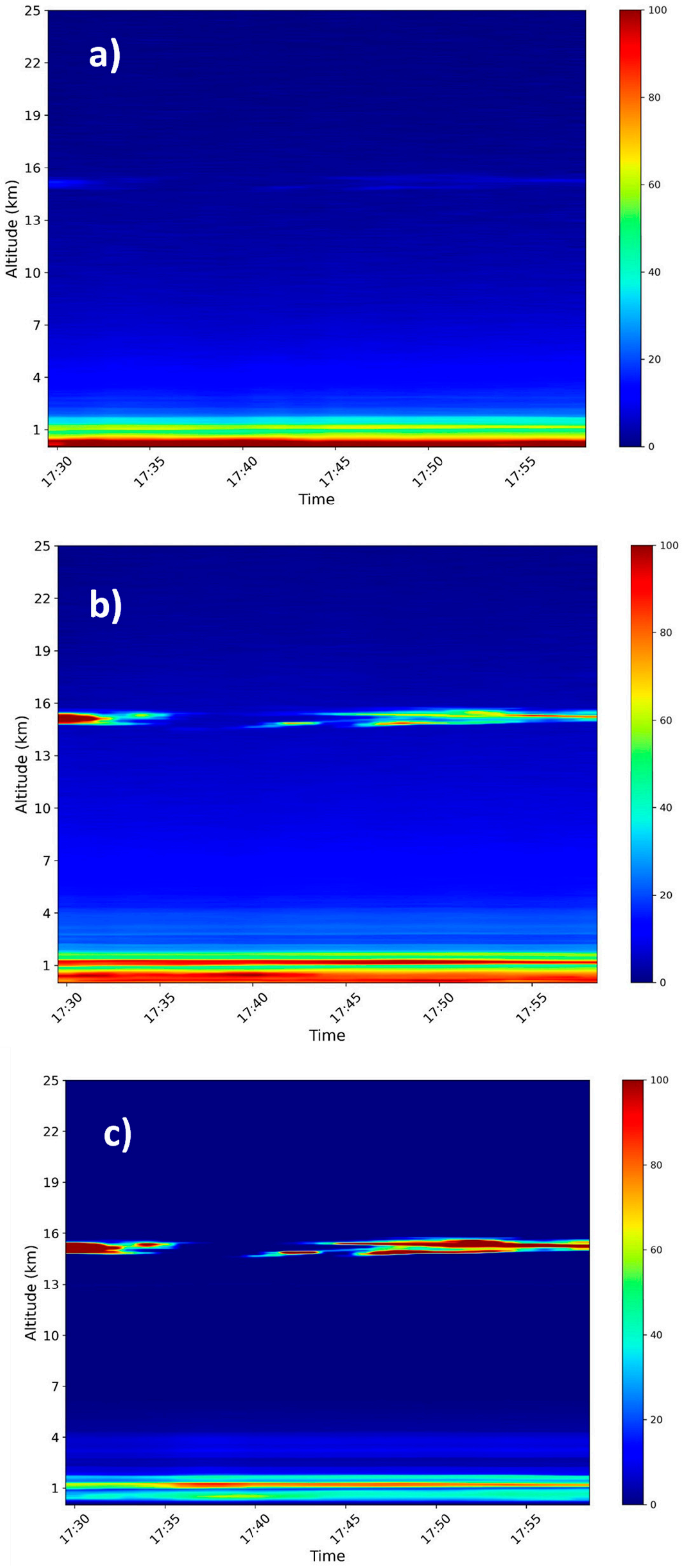

Figure 12. Colour maps of the lidar signals measured at 355 nm (a) 532 nm (b) and 1064 nm (c), showing the spatio-temporal variation of a thin cirrus layer observed in the atmospheric column up to 25 km of altitude.

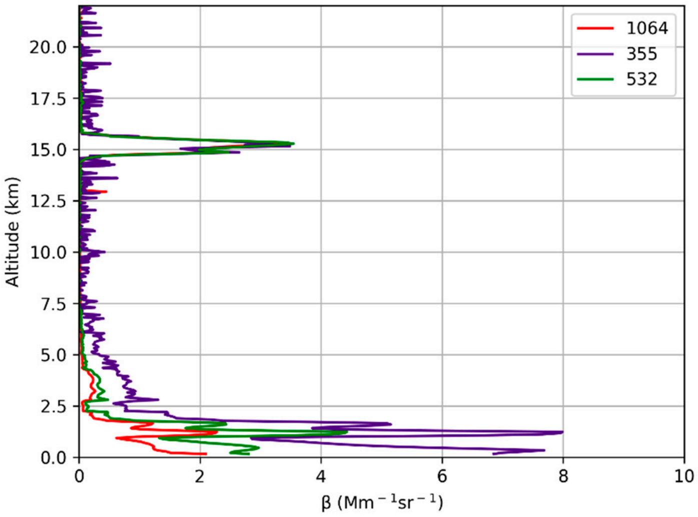

Figure 13. Aerosol backscattering coefficient profiles measure at 355 nm (purple line), 532 nm (green line) and 1064 nm (red line) from 17:30 to 18:00 UTC.

Table 1. Backscatter related Angstrom exponent obtained at different wavelengths (355 nm, 532 nm and 1064 nm).

λ_i/λ_j	BAE
355/532	0.03±0.13
355/1064	0.06±0.05
532/1064	0.08±0.06

3.1.6. Water Vapour Mixing Ratio measurement

The lidar echoes at 386 nm and 407 nm were used to obtain the water vapor mixing ratio (WVMR) profile by means of the Raman techniques [22]. This approach allows to obtain the WVMR from the ratio between the two lidar signals assuming a calibration constant that can be determined comparing lidar results with radiosonde derived WVMR profiles. The closeness of the airport to the lidar location doesn't permit the use of balloon-borne radiosonde. So we used Pratica di Mare radiosounding data taken at the time closest to the lidar observations, i.e. at 00:00 UTC. Figure 14 shows the comparison between the calibrated lidar profile and the one measured by the radiosonde. Despite the large distance between the two observational sites (about 240 km because the measurement tests were carried out in Naples) and the time difference between the measured profiles (about 6 hours), there was a good agreement, proving a correct spectral selection in the design of the lidar receiver.

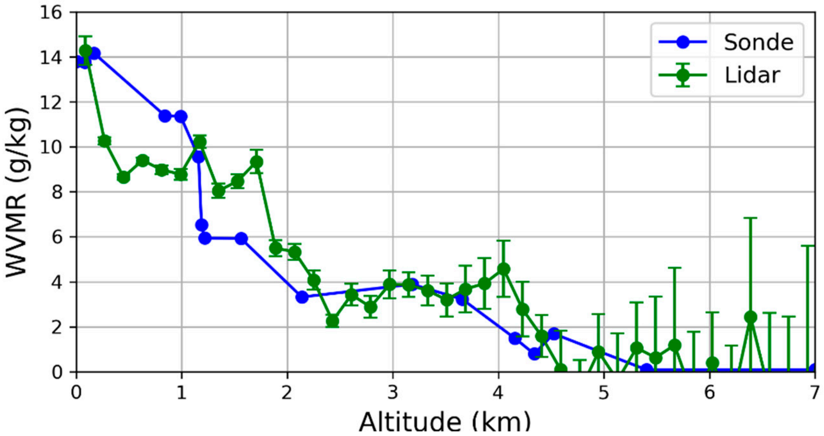

Figure 14. Water Vapour Mixing Ratio (g/Kg) derived by Raman lidar measurements (green line) and radiosounding data from Pratica di Mare (blue line). Error bars are reported only from lidar data due to the lack of the corresponding information for the radio-sounding data.

3.1.7. Lidar derived size distribution

The aerosol optical properties measured by lidar at different wavelengths (3 β and 2 α profiles) were used to retrieve the volume particle size distribution $dV(r)/dln(r)$ (expressed in a.u.). This was achieved using our inversion procedure based on a Bayesian model run with Monte Carlo simulations [33]. In particular, we used the averaged values of β(z) and α(z) over all the measured atmospheric column with the aim to compare lidar derived size distribution with the columnar size distribution provided by the AERONET sun-photometer data. Because the tests were carried out in the Naples ACTRIS National Facility, located at Napoli CeSMA (Centro Servizi Metrologici e tecnologici Avanzati), the involved sun-photometer was there sited (https://aeronet.gsfc.nasa.gov/cgi-bin/bamgomas_interactive, accessed on 17 January 2024).

The lidar-derived size distribution is reported in Figure 15a. The size distribution was obtained from lidar data taken at about 18:00 UTC and shows a bimodal shape with radius values at about 0.11 μm and 2.12 μm.

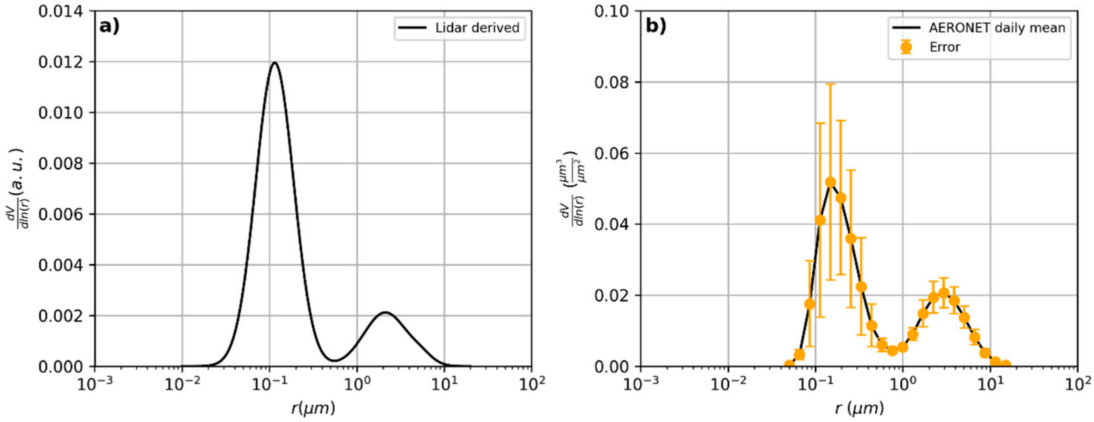

Figure 15. Particles size distribution retrieved by co-located measurements, taken by AERONET sun-photometer (a) and Lidar (b).

This lidar-derived size distribution shows fairly good agreement with the columnar particle size distribution provided by the AERONET sun-photometer as reported in Figure 15b. In this Figure, the columnar size distribution averaged over the day is shown together with the mean standard deviation that was used as data uncertainty. In particular, for the AERONET data taken at 14:19 UTC, the size distribution is bimodal, with the two mode radius values at about 0.15 µm and 2.94 µm, respectively. In our opinion, the differences between the mode radii of the two distributions are likely due to the different measure time.

4. Conclusions

A mobile Lidar system has been upgraded, tested and calibrated. The aim of such a new configuration, with the added capability to measure 3β, 2α and 2δ, was to increase the potential of the system to retrieve optical and microphysical properties of aerosol. The tests performed after specific calibration procedures showed, for each wavelength, very good lidar performances in terms of signal linearity, polarization and spectral calibration, WVMR and size distribution retrieving.

The test results relating to WVMR and volume particle size distribution were compared with ones obtained by different instrumentation, radio-sounding and AERONET sun-photometer respectively. The fair agreement of both the retrievals confirmed the ability of the upgraded system to more precisely characterize the aerosol optical and microphysical properties bringing the lidar to a configuration likely definable as "state of the art lidar".

Author Contributions: Conceptualization, M.M. A.B. and G.D.; methodology, M.M., A.B., S.S.; software, R.D., M.M.; formal analysis, M.M., R.D. and A.B.; investigation, S.C., G.A. and B.S.; resources, S.S.; writing—original draft preparation, A.B., M.M.; writing—review and editing, S.S., G.D.; visualization, M.M., R.D. and A.B.; supervision, A.B., S.S. "All authors have read and agreed to the published version of the manuscript."

Acknowledgments: The research leading to these results has received funding from the ITINERIS, Italian Integrated Environmental Research Infrastructures System (D.D. n. 130/2022 - CUP B53C22002150006) Funded by EU - Next Generation EU PNRR- Mission 4 "Education and Research" - Component 2: "From research to business" - In-vestment 3.1: "Fund for the realisation of an integrated system of research and innovation infrastructures". The authors thank ALA Advanced Lidar Applications s.r.l. for providing the PAPRICA software for the lidar microphysical properties retrieval. The Lidar was developed using funds of the VULCAMED and PON-GRINT projects of the Istituto Nazionale di Geofisica e Vulcanologia (INGV) and thanks to the support of F. Buongiorno, M. Coltelli, G. Puglisi.

References

1. Guffanti, M.; Ewert, J.W.; Gallina, G.M.; Bluth, G.J.S.; Swanson, G.L. Volcanic-Ash Hazard to Aviation during the 2003–2004 Eruptive Activity of Anatahan Volcano, Commonwealth of the Northern Mariana Islands. *Journal of Volcanology and Geothermal Research* **2005**, *146*, 241–255, doi:10.1016/j.jvolgeores.2004.12.011.
2. Blong, R.J. 2 - HAZARDS PRODUCED BY VOLCANIC ERUPTIONS. In *Volcanic Hazards*; Blong, R.J., Ed.; Academic Press: San Diego, 1984; pp. 14–69 ISBN 978-0-12-107180-6.
3. Horwell, C.J.; Baxter, P.J. The Respiratory Health Hazards of Volcanic Ash: A Review for Volcanic Risk Mitigation. *Bull Volcanol* **2006**, *69*, 1–24, doi:10.1007/s00445-006-0052-y.
4. Hirtl, M.; Arnold, D.; Baro, R.; Brenot, H.; Coltelli, M.; Eschbacher, K.; Hard-Stremayer, H.; Lipok, F.; Maurer, C.; Meinhard, D.; et al. A Volcanic-Hazard Demonstration Exercise to Assess and Mitigate the Impacts of Volcanic Ash Clouds on Civil and Military Aviation. *Natural Hazards and Earth System Sciences* **2020**, *20*, 1719–1739, doi:10.5194/nhess-20-1719-2020.
5. Witham, C.S.; Hort, M.C.; Potts, R.; Servranckx, R.; Husson, P.; Bonnardot, F. Comparison of VAAC atmospheric dispersion models using the 1 November 2004 Grimsvötn eruption. *Meteorological Applications* **2007**, *14*, 27–38, doi:10.1002/met.3.
6. Marzano, F.S.; Lamantea, M.; Montopoli, M.; Herzog, M.; Graf, H.; Cimini, D. Microwave Remote Sensing of the 2011 Plinian Eruption of the Grímsvötn Icelandic Volcano. *Remote Sensing of Environment* **2013**, *129*, 168–184, doi:10.1016/j.rse.2012.11.005.
7. Rolf, C.; Krämer, M.; Schiller, C.; Hildebrandt, M.; Riese, M. Lidar Observation and Model Simulation of a Volcanic-Ash-Induced Cirrus Cloud during the Eyjafjallajökull Eruption. *Atmospheric Chemistry and Physics* **2012**, *12*, 10281–10294, doi:10.5194/acp-12-10281-2012.
8. Lu, S.; Lin, H.X.; Heemink, A.; Segers, A.; Fu, G. Estimation of Volcanic Ash Emissions through Assimilating Satellite Data and Ground-Based Observations. *Journal of Geophysical Research: Atmospheres* **2016**, *121*, 10,971-10,994, doi:10.1002/2016JD025131.

9. Dacre, H.F.; Grant, A.L.M.; Hogan, R.J.; Belcher, S.E.; Thomson, D.J.; Devenish, B.J.; Marenco, F.; Hort, M.C.; Haywood, J.M.; Ansmann, A.; et al. Evaluating the Structure and Magnitude of the Ash Plume during the Initial Phase of the 2010 Eyjafjallajökull Eruption Using Lidar Observations and NAME Simulations. *J. Geophys. Res.* **2011**, *116*, D00U03, doi:10.1029/2011JD015608.
10. Mona, L.; Amodeo, A.; D'Amico, G.; Giunta, A.; Madonna, F.; Pappalardo, G. Multi-Wavelength Raman Lidar Observations of the Eyjafjallajökull Volcanic Cloud over Potenza, Southern Italy. *Atmospheric Chemistry and Physics* **2012**, *12*, 2229–2244, doi:10.5194/acp-12-2229-2012.
11. Wiegner, M.; Gasteiger, J.; Groß, S.; Schnell, F.; Freudenthaler, V.; Forkel, R. Characterization of the Eyjafjallajökull Ash-Plume: Potential of Lidar Remote Sensing. *Physics and Chemistry of the Earth, Parts A/B/C* **2012**, *45–46*, 79–86, doi:10.1016/j.pce.2011.01.006.
12. Sicard, M. Monitoring of the Eyjafjallajökull Volcanic Aerosol Plume over the Iberian Peninsula by Means of Four EARLINET Lidar Stations. *Atmospheric Chemistry and Physics* **2012**.
13. Pappalardo, G.; Amodeo, A.; Mona, L.; Pandolfi, M.; Pergola, N.; Cuomo, V. Raman Lidar Observations of Aerosol Emitted during the 2002 Etna Eruption. *Geophysical Research Letters* **2004**, *31*, doi:10.1029/2003GL019073.
14. Pappalardo, G.; Mona, L.; D'Amico, G.; Wandinger, U.; Adam, M.; Amodeo, A.; Ansmann, A.; Apituley, A.; Alados Arboledas, L.; Balis, D.; et al. Four-Dimensional Distribution of the 2010 Eyjafjallajökull Volcanic Cloud over Europe Observed by EARLINET. *Atmospheric Chemistry and Physics* **2013**, *13*, 4429–4450, doi:10.5194/acp-13-4429-2013.
15. Pisani, G.; Boselli, A.; Coltelli, M.; Leto, G.; Pica, G.; Scollo, S.; Spinelli, N.; Wang, X. Lidar Depolarization Measurement of Fresh Volcanic Ash from Mt. Etna, Italy. *Atmospheric Environment* **2012**, *62*, 34–40, doi:10.1016/j.atmosenv.2012.08.015.
16. Mereu, L.; Scollo, S.; Mori, S.; Boselli, A.; Leto, G.; Marzano, F. Maximum-Likelihood Retrieval of Volcanic Ash Concentration and Particle Size From Ground-Based Scanning Lidar. *IEEE Transactions on Geoscience and Remote Sensing* **2018**, *PP*, 1–19, doi:10.1109/TGRS.2018.2826839.
17. Klett, J.D. Stable Analytical Inversion Solution for Processing Lidar Returns. *Appl. Opt., AO* **1981**, *20*, 211–220, doi:10.1364/AO.20.000211.
18. Fernald, F.G. Analysis of Atmospheric Lidar Observations: Some Comments. *Appl. Opt., AO* **1984**, *23*, 652–653, doi:10.1364/AO.23.000652.
19. Ansmann, A.; Riebesell, M.; Wandinger, U.; Weitkamp, C.; Voss, E.; Lahmann, W.; Michaelis, W. Combined Raman Elastic-Backscatter LIDAR for Vertical Profiling of Moisture, Aerosol Extinction, Backscatter, and LIDAR Ratio. *Appl. Phys. B* **1992**, *55*, 18–28, doi:10.1007/BF00348608.
20. Ansmann, A.; Riebesell, M.; Weitkamp, C. Measurement of Atmospheric Aerosol Extinction Profiles with a Raman Lidar. *Opt Lett* **1990**, *15*, 746–748, doi:10.1364/ol.15.000746.
21. Alvarez, J.M.; Vaughan, M.; Hostetler, C.A.; Hunt, W.; Winker, D.M. Calibration Technique for Polarization-Sensitive LIDARs. *Journal of Atmospheric and Oceanic Technology - J ATMOS OCEAN TECHNOL* **2006**, *23*, doi:10.1175/JTECH1872.1.
22. Whiteman, D. Examination of the Traditional Raman Lidar Technique. II. Evaluating the Ratios for Water Vapor and Aerosols. *Applied optics* **2003**, *42*, 2593–2608, doi:10.1364/AO.42.002593.
23. Vérèmes, H.; Payen, G.; Keckhut, P.; Duflot, V.; Baray, J.-L.; Cammas, J.-P.; Evan, S.; Posny, F.; Körner, S.; Bosser, P. Validation of the Water Vapor Profiles of the Raman Lidar at the Maïdo Observatory (Reunion Island) Calibrated with Global Navigation Satellite System Integrated Water Vapor. *Atmosphere* **2019**, *10*, 713, doi:10.3390/atmos10110713.
24. Burton, S.; Chemyakin, E.; Liu, X.; Knobelspiesse, K.; Stamnes, S.; Sawamura, P.; Moore, R.; Hostetler, C.; Ferrare, R. Information Content and Sensitivity of the 3β + 2α Lidar Measurement System for Aerosol Microphysical Retrievals. *Atmospheric Measurement Techniques Discussions* **2016**, 1–39, doi:10.5194/amt-2016-240.
25. Snels, M.; Cairo, F.; Colao, F.; Di Donfrancesco, G. Calibration Method for Depolarization Lidar Measurements. *International Journal of Remote Sensing* **2009**, *30*, 5725–5736, doi:10.1080/01431160902729572.
26. Pal, S.R.; Carswell, A.I. Polarization Properties of Lidar Backscattering from Clouds. *Appl. Opt., AO* **1973**, *12*, 1530–1535, doi:10.1364/AO.12.001530.
27. Wang, X.; Boselli, A.; Sannino, A.; Song, C.; Spinelli, N.; Zhao, Y.; Pan, C. Calibration of Multi-Wavelength Raman Polarization Lidar. *EPJ Web of Conferences* **2015**, *89*, 01002, doi:10.1051/epjconf/20158901002.

28. Wandinger, U.; Ansmann, A. Experimental Determination of the Lidar Overlap Profile with Raman Lidar. *Appl Opt* **2002**, *41*, 511–514, doi:10.1364/ao.41.000511.
29. Hey, J.V.; Coupland, J.; Foo, M.H.; Richards, J.; Sandford, A. Determination of Overlap in Lidar Systems. *Appl. Opt., AO* **2011**, *50*, 5791–5797, doi:10.1364/AO.50.005791.
30. Povey, A.; Grainger, R.; Peters, D.; Agnew, J.L.; Rees, D. Estimation of a Lidar's Overlap Function and Its Calibration by Nonlinear Regression. *Applied optics* **2012**, *51*, 5130–5143, doi:10.1364/AO.51.005130.
31. Freudenthaler, V.; Linné, H.; Chaikovski, A.; Rabus, D.; Groß, S. EARLINET Lidar Quality Assurance Tools. *Atmospheric Measurement Techniques Discussions* **2018**, 1–35, doi:10.5194/amt-2017-395.
32. Voudouri, K.; Giannakaki, E.; Komppula, M.; Balis, D. Variability in Cirrus Cloud Properties Using a PollyXT Raman Lidar over High and Tropical Latitudes. *Atmospheric Chemistry and Physics* **2020**, *20*, 4427–4444, doi:10.5194/acp-20-4427-2020.
33. Sorrentino, A.; Sannino, A.; Spinelli, N.; Piana, M.; Boselli, A.; Tontodonato, V.; Castellano, P.; Wang, X. A Bayesian Parametric Approach to the Retrieval of the Atmospheric Number Size Distribution from Lidar Data. *Atmospheric Measurement Techniques* **2022**, *15*, 149–164, doi:10.5194/amt-15-149-2022.